

## PSR J0357+3205: the tail of the turtle

M. Marelli,<sup>1</sup> A. De Luca,<sup>1,2</sup> D. Salvetti,<sup>1,2,3</sup> N. Sartore,<sup>1</sup> A. Sartori,<sup>1,2,3</sup> P. Caraveo<sup>1,2</sup>, F.  
Pizzolato<sup>1</sup>, P.M. Saz Parkinson<sup>4</sup> and A. Belfiore<sup>1,4</sup>

marelli@iasf-milano.inaf.it

Received \_\_\_\_\_; accepted \_\_\_\_\_

arXiv:1212.6664v1 [astro-ph.HE] 29 Dec 2012

---

<sup>1</sup>INAF - Istituto di Astrofisica Spaziale e Fisica Cosmica Milano, via E. Bassini 15, 20133  
Milano, Italy

<sup>2</sup>Istituto Nazionale di Fisica Nucleare, Sezione di Pavia, Via Bassi 6, I-27100 Pavia (Italy)

<sup>3</sup>Università degli Studi di Pavia, Strada Nuova 65, 27100 Pavia, Italy

<sup>4</sup>Santa Cruz Institute for Particle Physics, University of California, Santa Cruz, CA 95064

## ABSTRACT

Using a new *XMM-Newton* observation, we have characterized the X-ray properties of the middle-aged radio-quiet  $\gamma$ -ray pulsar J0357+3205 (named Morla) and its tail. The X-ray emission from the pulsar is consistent with a magnetospheric non-thermal origin plus a thermal emission from a hot spot (or hot spots). The lack of a thermal component from the whole surface makes Morla the coldest neutron star in its age range. We found marginal evidence for a double-peaked modulation of the X-ray emission. The study of the 9'-long tail confirmed the lack of extended emission near the pulsar itself. The tail shows a very asymmetric brightness profile and its spectrum lacks any spatial variation. We found the nebular emission to be inconsistent with a classical bow-shock, ram-pressure dominated pulsar wind nebula. We propose thermal bremsstrahlung as an alternative mechanism for Morla's tail emission. In this scenario, the tail emission comes from the shocked interstellar medium (ISM) material heated up to X-ray temperatures. This can fully explain the peculiar features of the tail, assuming a hot, moderately dense interstellar medium around the pulsar. For a bremsstrahlung-emitting tail, we can estimate the pulsar distance to be between 300 and 900 pc. A pulsar velocity of  $\sim 1900$  km s $^{-1}$  is required - which would make Morla the pulsar with the largest velocity - and high inclination angles ( $>70^\circ$ ) are preferred. We propose Morla's nebula as the first example of a new "turtle's tail" class of thermally-emitting nebulae associated to high velocity pulsars.

*Subject headings:* Stars: neutron — Pulsars: general — Pulsars: individual (PSR J0357+3205) — X-rays: stars

## 1. Introduction

The dramatic increase in the number of known gamma-ray pulsars since the launch of the *Fermi Gamma-ray Space Telescope* offers the first opportunity to study a sizeable population of these high-energy sources. The *Fermi* Large Area Telescope (LAT, Atwood et al. (2009)) has discovered pulsed  $\gamma$ -ray signals from more than 100 objects (Abdo et al. 2010a; LAT collaboration in preparation), revolutionizing our view of them and marking the birth of new high-energy pulsar sub-families, such as millisecond (Abdo et al. 2009a) and radio-quiet  $\gamma$ -ray pulsars (Abdo et al. 2009b), that are as numerous as the classical one. The wealth of detections confirms the importance of the  $\gamma$ -ray channel in the overall energy budget of rotation-powered pulsars and points to emission models in which the  $\gamma$ -ray production occurs in the outer magnetosphere along open-field lines (outer gap/slot gap, Cheng et al. (1986); Harding & Muslimov (2004)) and paves the way for our understanding of the three-dimensional structure and electrodynamics of neutron star magnetospheres.

In a sense, the most important objects to constrain pulsar models are the “extreme” ones, accounting for the tails of the population distribution in energetics, age and magnetic field. In this respect, PSR J0357+3205 is one of the most interesting pulsars discovered by the LAT. J0357+3205, which we name “Morla” (cf. “The Neverending Story”, M. Ende) for its slow rotation among *Fermi*-LAT pulsars (P=444 ms), was discovered in a blind search during the first three months of *Fermi*-LAT scanning (Abdo et al. 2009c). It is located off the Galactic plane, at a latitude of  $b \simeq -16^\circ$ . While Morla is not the oldest rotation-powered pulsar ( $\tau_c = 5.4 \times 10^5$  yr) - with an age similar to the well-known “Three Musketeers” (De Luca et al. 2005) - it is the slowest rotator among *Fermi* pulsars. Its spin-down luminosity, as low as  $\dot{E}_{rot} = 5.9 \times 10^{33}$  erg s $^{-1}$ , makes it one of the non-recycled  $\gamma$ -ray pulsars with the smallest rotational energy loss detected so far. This suggests that

PSR J0357+3205 is quite nearby: by scaling its  $\gamma$ -ray flux using the “pseudo-distance” relation from Saz Parkinson et al. (2010), we obtain a distance of  $\sim 500$  pc, making Morla a natural target for X-ray observations.

Exploiting a joint *Chandra* and *NOAO* program, De Luca et al. (2011) found the X-ray counterpart of the  $\gamma$ -ray pulsar to be located at R.A.(J2000) =  $03^h57^m52^s.32$ , Dec.(J2000) =  $+32^\circ05'20.6''$  ( $0.25''$  error radius, 68% confidence level). The pulsar X-ray emission was found to be consistent with a purely magnetospheric, non-thermal origin leading to a value of the  $\gamma$ -to-X flux ratio of  $\sim 1000$ , well below the mean for radio-quiet pulsars ( $\sim 9000$ , Marelli (2012)). Unfortunately, the poor statistics precluded a clear detection of a thermal component in the neutron star spectrum as well as a full characterization of its column density and distance. Nevertheless, the *Chandra* data unveiled the presence of an extended structure protruding from the pulsar and extending  $>9'$  in length, which would correspond to  $\sim 1.3$  pc for a pulsar distance of 500 pc, and  $\sim 1.5'$  in width. The “tail” is apparently detached from the pulsar, without detection of nebular counts until  $50''$  from the pulsar; it shows an unusual, asymmetric morphology, with the brightest part far from the pulsar. *NOAO* optical images, taken in V and K bands, show no hints of correlated, diffuse emission. No extended source was detected either in public radio or infrared surveys. The lack of any  $H\alpha$  emission around the pulsar (De Luca et al. in preparation) points to a full ionized, likely hot ( $> 10^4$  K), ISM.

Recently, using a new *Chandra* observation, De Luca et al. (in preparation) detected the pulsar’s proper motion of  $165 \pm 30$  mas yr $^{-1}$ , in the direction away from the tail and parallel to the Galactic plane. Assuming a pulsar distance of 500 pc, this results in a lower limit velocity of 390 km s $^{-1}$ , making it a relatively high-velocity pulsar (Manchester et al. 2005). Many extended tails of X-ray emission have been discovered, associated with a number of rotation powered pulsars (e.g. Kargaltsev et al. (2008)) within the framework of a ram-pressure dominated pulsar wind nebula (see Gaensler & Slane (2006) for a review).

However, the unusual phenomenology of the feature we observed is barely consistent with such a picture. There is no hint of diffuse emission in the pulsar surroundings, where bright emission from the wind termination shock should be seen (as observed in other known cases). Moreover, the asymmetric brightness profile of the tail, with its sharp north-eastern edge and its broad maximum at large distance from the pulsar is remarkably different from any other observed structure (with the possible exception of the peculiar feature associated with PSR B2224+65, powering the Guitar nebula - see Hui & Becker (2007)). The mere existence of the tail is also problematic for a pulsar with such a low  $\dot{E}_{rot}$  as J0357+3205 (see e.g. Jager & Djannati-Atai (2008)).

In order to assess the nature of the tail and its relationship with the pulsar, as well as to better constrain the pulsar emission properties and physics, we obtained a deep observation of the pulsar and its peculiar tail with *XMM-Newton*. Exploiting its high spectral resolution, we were able to disentangle the components of the pulsar spectrum and constrain its distance based on the absorption column density. A complete study of the timing behavior of Morla in X-rays was carried out as well. Finally, we studied the properties of the tail, in order to characterize the mechanisms responsible for its emission.

## 2. Observations and Data Reduction

Our deep *XMM-Newton* observation of Morla started on 2011 September 15 at 02:37:18 UT and lasted 111.3 ks. The PN camera (Struder et al. 2001) of the EPIC instrument was operating in Large Window mode (time resolution of 47.7 ms over a  $14' \times 27'$  field of view (FOV)), while the MOS detectors (Turner et al. 2001) were set in full frame mode (2.6 s time resolution on a  $15'$  radius FOV). The thin optical filter was used for the PN camera while we chose to use the medium filter for the MOS detectors due to the presence of moderately bright ( $m_R \sim 9$ ) stars. We used the *XMM-Newton* Science Analysis

Software (SAS) v11.0. After standard data processing, using the `eprocc` and `emproc` tools, and screening for high particle background time intervals (following De Luca & Molendi (2004)), the good, dead-time corrected exposure time was 98.5 ks for the PN and 108.3 ks for the two MOS detectors. In order to fully characterize both the pulsar and the nebula, we also used the three available *Chandra*/ACIS (Garmire et al. 2003) observations of the field, performed on 2009 October 25, 26, and 2011 December 25, lasting 29.5, 47.1, and 29.0 ks respectively (these data sets were included in the investigations by De Luca et al. (2011) and De Luca et al. (in preparation)). We retrieved “level 2” data from the *Chandra* Science Archive and used the *Chandra* Interactive Analysis of Observation (CIAO) software v.4.2. We also combined the *Chandra* spectra, response matrices and effective area files using the `mathpha`, `addarf` and `addrmf` tools.

## 2.1. Imaging and Source Detection

Figure 1 shows the 0.3-6 keV exposure-corrected *XMM-Newton* FOV image, where the PN and two MOS images were added with the `ximage` tool. We applied a Gaussian filter with a kernel radius of 5”. The image clearly shows the straylight effect, probably due to the bright source X Persei that dominates the X-ray sky  $\sim 70'$  to the southwest of Morla, with a flux of  $\sim 10^{-9}$  erg cm $^{-2}$  s $^{-1}$ . X-ray straylight in EPIC is produced by photons which experience single reflection by the mirror hyperbolae and which reach the sensitive area of the camera and produce near-annular structures in the image. In order to study the background sources in the *XMM-Newton* observation, we evaluated the spectrum of our straylight annuli. This is consistent, at low energies, with the X Persei spectrum found by La Palombara & Mereghetti (2007), thus we added and froze these components in the spectral model of sources affected by this phenomenon.

Source detection using maximum likelihood fitting was done simultaneously on each

of the EPIC-PN, MOS1, and MOS2 using the SAS tool `edetect_chain`. This tool runs on the event lists and invokes several other SAS tools to produce background, sensitivity, and vignetting-corrected exposure maps. A likelihood threshold of 10 was used for source detection, corresponding to a significance level of  $3.6\sigma$ . Figure 1 shows the brightest sources in the PN field of view; they were analyzed in order to produce X-ray spectra and find optical counterparts. The first 7 objects were also observed by Chandra so that we used both the telescope datasets to obtain radial profiles and spectra.

First, we analyzed their radial brightness profile and compared them with the *XMM-Newton* and *Chandra* theoretical Point Spread Functions (PSFs). We found sources 8 and 14 to be the superimposition of two different point-like sources. Using the 2011 Chandra data, source 7 is incompatible with a simple point-like source. This is in agreement with results from XMM-Newton data - though heavily affected by straylight photons - of a point-like source surrounded by extended emission. The NASA/IPAC Extragalactic Database (NED<sup>1</sup>) reports one radio source compatible with the point-like emission, identifying it as an Active Galactic Nucleus (AGN) in a cluster.

Each spectrum was then fitted either with an absorbed powerlaw, well-suited for AGNs as well as pulsars and an absorbed `appec`, well-suited for stellar coronae. Only source 9 requires a double `appec`, quite common for stellar coronae; for this source we thus cannot exclude the superimposition of two different stars closer than  $\sim 2''$ . Three sources (11, 13, and 14) cannot be described by the simple models considered here; deeper studies on the serendipitous sources are beyond the aim of this paper so they were excluded from our analysis.

Optical counterparts were searched in the deep (4hr 26min exposure) optical and near-infrared images collected with the 4m Mayall Telescope on 2009 November 10, using the

---

<sup>1</sup><http://ned.ipac.caltech.edu/>

large-field ( $36' \times 36'$ ) Mosaic CCD Imager (Jacoby et al. 1998). All the results of our X-ray and optical analyses on background sources are reported in Table 1.

We found 2 sources (8 and 9) that are compatible with a star interpretation both in the X-ray and optical bands. These two objects are likely located closer to us than Morla, given their lower value of the absorption column. Deeper optical observations with different filters would be required to find their distances from the optical absorption. All the remaining objects are extragalactic, while source 17 presents a very high value of the X-ray to optical flux ratio. This can be described as an obscured AGN (Mainieri et al. 2002). It is possible that the emission actually comes from two different sources (thus lowering the X-ray to optical flux ratio), though the low statistics prevent us from studying the brightness profile of the source.

All the AGNs were fitted together, linking their  $N_H$  to assess the average Galactic absorption column. The resulting Galactic value  $N_H^{gal} = 2.10 \pm 0.09 \times 10^{21} \text{ cm}^{-2}$  is in good agreement with the theoretical one predicted by Dickey & Lockman (1990) and Kalberla et al. (2005) for objects at the limit of the Galaxy ( $\sim 500 \text{ pc}$ ).

### 3. The Pulsar

#### 3.1. Pulsar Spectral Analysis

In order to optimize the pulsar extraction radius we evaluated the brightness profile of the source to maximize both the signal-to-noise ratio (S/N) and the number of counts. The PSF of the EPIC-PN camera onboard *XMM-Newton* is best described by an off-axis, energy-dependent King function (Read 2004). The full width half maximum of the PSF for an on-axis source at 1.5 keV is typically less than  $12.5''$  for the PN camera and  $4.4''$



Table 1: X-ray and optical analysis of background sources

Object	Coordinates <sup>a</sup>	spec <sub>X</sub>	N <sub>H</sub> (10 <sup>21</sup> cm <sup>-2</sup> )	F <sub>X</sub> /F <sub>O</sub>	type
1	03:57:47.50,+32:03:45.10	pow	1.83±0.20	5.0	AGN
2	03:57:50.95,+32:01:47.70	pow/apec	2.11 <sup>+1.20</sup> / <sub>-1.02</sub> /1.36 <sup>+0.87</sup> / <sub>-0.71</sub>	6.5	AGN
3	03:57:53.90,+32:00:58.50	pow/apec	1.02 <sup>+1.11</sup> / <sub>-0.97</sub> /0.66 <sup>+0.46</sup> / <sub>-0.66</sub>	9.1	AGN
4	03:58:21.95,+31:59:11.65	pow	1.87±0.22	1.8	AGN
5	03:58:15.25,+32:00:17.35	pow	1.91 <sup>+0.66</sup> / <sub>-0.58</sub>	1.0	AGN
6	03:58:00.29,+31:58:01.90	pow/apec	2.97 <sup>+1.29</sup> / <sub>-1.03</sub> /2.00 <sup>+0.91</sup> / <sub>-0.66</sub>	1.5	AGN
7	03:57:39.35,+32:01:03.00	pow/apec	2.68±0.60/1.20 <sup>+0.38</sup> / <sub>-0.34</sub>	9.2	AGN
8a	03:57:12.7,5+32:00:50.10	apec	1.25 <sup>+0.76</sup> / <sub>-0.68</sub>	0.0056	Star
8b	03:57:12.95,+32:00:42.65	apec	0.49 <sup>+0.25</sup> / <sub>-0.22</sub>	0.0028	Star
9	03:57:07.35,+32:02:59.65	2apec	0.21 <sup>+0.12</sup> / <sub>-0.11</sub>	0.0060	Star
10	03:57:46.30,+31:57:24.50	pow	1.98 <sup>+0.64</sup> / <sub>-0.92</sub>	3.6	AGN
12	03:57:20.20,+32:03:14.95	pow/apec	1.69 <sup>+0.54</sup> / <sub>-0.60</sub> /0.98 <sup>+0.41</sup> / <sub>-0.35</sub>	0.12	AGN
15	03:58:40.80,+32:02:27.35	pow	1.87 <sup>+0.46</sup> / <sub>-0.50</sub>	2.8	AGN
16	03:58:20.35,+32:08:24.85	pow	1.83 <sup>+1.27</sup> / <sub>-1.11</sub>	1.0	AGN
17	03:58:17.45,+32:08:50.20	pow/apec	1.73±0.72/0.94 <sup>+0.49</sup> / <sub>-0.41</sub>	400	AGN

<sup>a</sup>We report the R.A., Dec. (J2000) coordinates of the optical counterpart, with a typical error of 0.3". If there was no optical counterpart, X-ray coordinates are shown, with a typical systematic error of 2" and 1 $\sigma$  statistical error of  $\sim 1$ ".

Note. — X-ray and optical parameters of the brightest sources in the PN field of view; the colors are in a logarithmic scale. All the errors are at a 90% confidence level. We use both the optical to X-ray flux ratio and the X-ray spectral type to separate AGNs from stellar coronal emissions. PSF studies show that sources 8 and 14 result from the superimposition of two sources while source 9 can be a single source. The spectra of sources 11, 13, and 14 cannot be described by a powerlaw nor apec components. Source 17 could be associated with an obscured AGN (Mainieri et al. 2002).

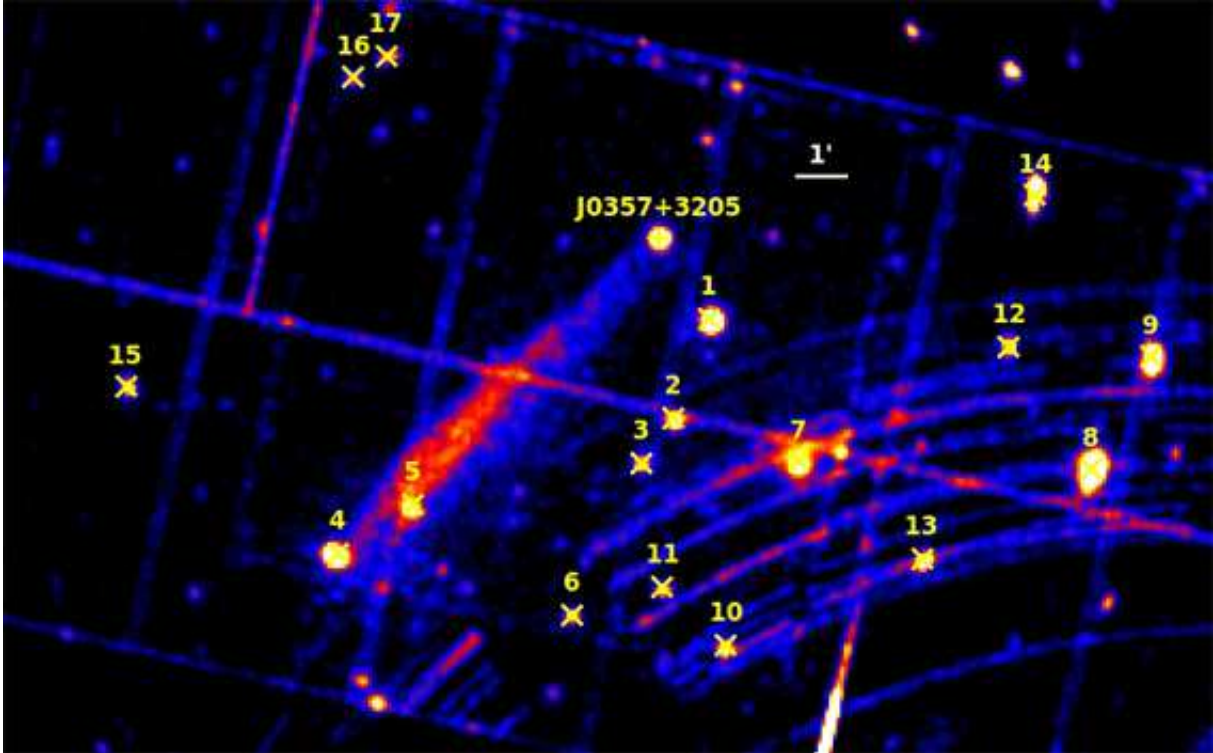


Fig. 1.— Combined 0.3-6 keV exposure-corrected *XMM-Newton* field of view, where the PN and two MOS images were added with `ximage` tool. We applied a gaussian filter with a kernel radius of  $5''$ . The yellow crosses mark the serendipitous sources we analyzed to constrain the value of the Galactic absorption column (see Table 1). In the lower-right part of the figure the straylight effect is apparent.

for the two MOS detectors<sup>2</sup>. Our results are in agreement with those published by De Luca et al. (2011), based on *Chandra* data, with no excesses within  $\sim 30''$  of the pulsar, with the exception of its bright tail. We found the best extraction radius to be  $18''$ , containing 2022, 515 and 540 counts in the 0.3-10 keV energy range in the PN and the two MOS detectors respectively, with a background contribution of  $\sim 10\%$ . We generated an ad hoc response matrix and effective area files using the SAS tools `rmfgen` and `arfgen`. We also analyzed the *Chandra* spectra of the source using a  $1.5''$  extraction radius (698 pulsar counts with a background contribution of 0.4%); we added the three different spectra with the tool `mathpha`. Response matrix and effective area files were generated using the CIAO script `psextract`. Due to the presence of the pulsar tail, backgrounds were evaluated from a circle on the same CCD as the pulsar and without serendipitous X-ray sources, with a radius of  $10''$  for *Chandra* and  $50''$  for the XMM telescopes.

For the pulsar emission, we tried a simple powerlaw (pow), the combination of a powerlaw and a blackbody (bb) as well as the combination of a powerlaw and a magnetized neutron star atmosphere model (`nsa` in XSpec - assuming a neutron star with a radius of 13 km, mass of  $1.4 M_{\odot}$  and a surface magnetic field of  $10^{13}$  G). While the simple powerlaw gives a fit only marginally acceptable (reduced chi square  $\chi_{\nu}^2=1.22$ , 134 degrees of freedom (dof)), both the composite models yield better fits (`nsa+pow`:  $\chi_{\nu}^2=0.96$ , 131 dof; `bb+pow`  $\chi_{\nu}^2=0.97$ , 132 dof). An F-test performed comparing a simple powerlaw with the composite spectra results in a chance probability of less than  $10^{-7}$ , pointing to a significant improvement from adding a thermal component. The pulsar emission is well described by a powerlaw component with a photon index of  $\Gamma = 2.28_{-0.16}^{+0.17}$  (90% confidence errors) and a blackbody component with a temperature of  $kT = 94.0_{-9.2}^{+12.1}$  eV and an emitting radius at  $R = 0.45_{-0.19}^{+0.31} d_{500}$  km (where  $d_{500}$  is the distance of the pulsar in units of 500 pc), absorbed

---

<sup>2</sup>[http://xmm.esac.esa.int/external/xmm\\_user\\_support/documentation/sas\\_usg/USG/](http://xmm.esac.esa.int/external/xmm_user_support/documentation/sas_usg/USG/)

by a column density of  $N_H = 1.20_{-0.45}^{+0.52} \times 10^{21} \text{ cm}^{-2}$ . The 0.3-10 keV non-thermal pulsar luminosity is  $L_{nth} = 1.63_{-0.28}^{+0.06} d_{500}^2 \times 10^{30} \text{ erg s}^{-1}$ , while the thermal one  $L_{nth} = 1.14_{-0.20}^{+0.04} d_{500}^2 \times 10^{30} \text{ erg s}^{-1}$ . As expected, the `nsa` model yields a lower temperature of  $41.1_{-6.2}^{+8.9} \text{ eV}$  and a larger emitting radius of  $R = 3.77_{-2.08}^{+4.18} d_{500} \text{ km}$ , and a powerlaw component with  $\Gamma = 2.21 \pm 0.19$ , absorbed by a column density of  $N_H = 1.49_{-0.53}^{+0.59} \times 10^{21} \text{ cm}^{-2}$ . Both results are in agreement with the upper limits on the thermal components found by De Luca et al. (2011). Figure 2 shows the results of the fit for the two different spectral models.

### 3.2. Pulsar Timing Analysis

In order to carry out a proper timing analysis with EPIC data, a correct photon arrival time must be assigned to each event detected on board. The transformation from readout sequences by the EPIC camera to photon arrival times of each photon is performed by the EPEA (European Photon Event Analyser, Kuster et al. (1999)). A problem in the EPEA can produce time jumps in some observations, which have to be corrected. In order to identify any possible remaining time jumps, one must neglect both the barycentering and the randomization of photon arrival times. The time  $\Delta t$  between successive events is then calculated and divided by the Frame Time (FT) of the relevant mode (47.66384 ms for PN Large Window mode). A time jump is shown to exist when  $\Delta t/\text{FT}$  is different from an integer by a quantity larger than a tolerance parameter. Only those time jumps which happen to be an integer multiple of the relevant FT would be missed by this method (see e.g. Marelli (2012)).

Our *XMM-Newton* data show that a time jump happened in all the three instruments between 2011-09-15 16:04:45.822 and 16:10:14.310 UTC, at about the half of the observation. Such event makes it more difficult to find the pulsation of Morla, creating a possible misalignment in the pulsar phase assigned to the photons before and after the jump. For

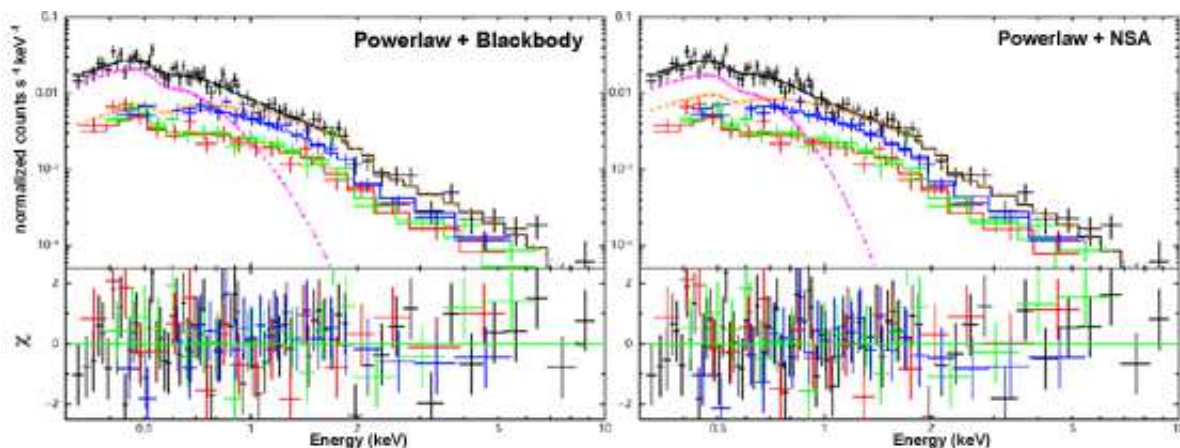


Fig. 2.— PN and MOS spectra of the Morla pulsar. Pattern 0-4 PN events and pattern 0-12 MOS events have been selected among photons within  $18''$  of the target position. The spectra are rebinned in order to have at least 25 counts per bin. The black, red, and green curves show the data from the PN and two MOS detectors, respectively. Also shown are the spectral fits: magenta curves show the thermal components, while orange curves the non-thermal ones. The data in the left panel are fitted with an absorbed powerlaw plus a blackbody while the data in the right panel use an absorbed powerlaw plus neutron star atmosphere (nsa) model. The lower panels show the residuals, in units of standard deviations, with 1 standard deviation error bars.

this reason, we performed careful timing studies in the two subsets, as well as in the total data set.

We evaluated the optimal selection of pulsar events by maximizing the signal-to-noise ratio in the 0.2-6 keV energy range as a function of the source extraction region. The optimal choice turned out to be a source extraction radius of 18" for the PN camera. We selected only pattern 0 photons in the range 0.2-0.35 keV in order to reduce the background contribution due to low-energy electronic noise, while in the 0.35-6 keV energy range, we used pattern 0-4 photons. Photon arrival times were converted to the solar system barycenter using the SAS tool `barycen`. According to the accurate *Fermi*-LAT ephemeris (LAT collaboration in preparation), a period of  $P = 0.44410548661(9)$  s is expected at the epoch of the XMM observation (the uncertainty on the last digit is computed by propagating the  $3\sigma$  error of the *Fermi*-LAT timing solution). The uncertainty of  $\sim 10^{-10}$  s is much smaller than the intrinsic resolution of the *XMM-Newton* dataset ( $P^2/2\Delta t \sim 8.4 \times 10^{-7}$  s). Thus, if the spin-down of the pulsar is stable, a single trial folding is appropriate. Folding using the full LAT ephemeris yields marginal evidence for a modulation of the X-ray emission (see Figure 3). A Pearson's  $\chi^2$  test on the folded light curve (10 phase bins) in the 0.2-6 keV energy range results in a probability of  $5 \times 10^{-4}$  of sampling a uniform distribution. Due to the low signal modulation, a study of the phase-misalignment before and after the time jump was not possible. To evaluate the significance of the detection independently of the phase binning chosen, we computed the corresponding  $Z^2$  value using the Rayleigh test (Buccheri et al. 1983) for 1 and 2 harmonics. This exercise yields probabilities as small as  $5 \times 10^{-4}$  and  $3 \times 10^{-6}$ , respectively, for a chance fluctuation. Such a test confirms the hint of a modulation at the pulsar frequency (and its first harmonic) in the *XMM-Newton* data, with a misalignment between the X-ray and gamma-ray peaks (see Figure 3). However, the low number of counts prevented us from disentangling the thermal from the non-thermal pulsation or from performing a phase-resolved spectroscopy analysis.

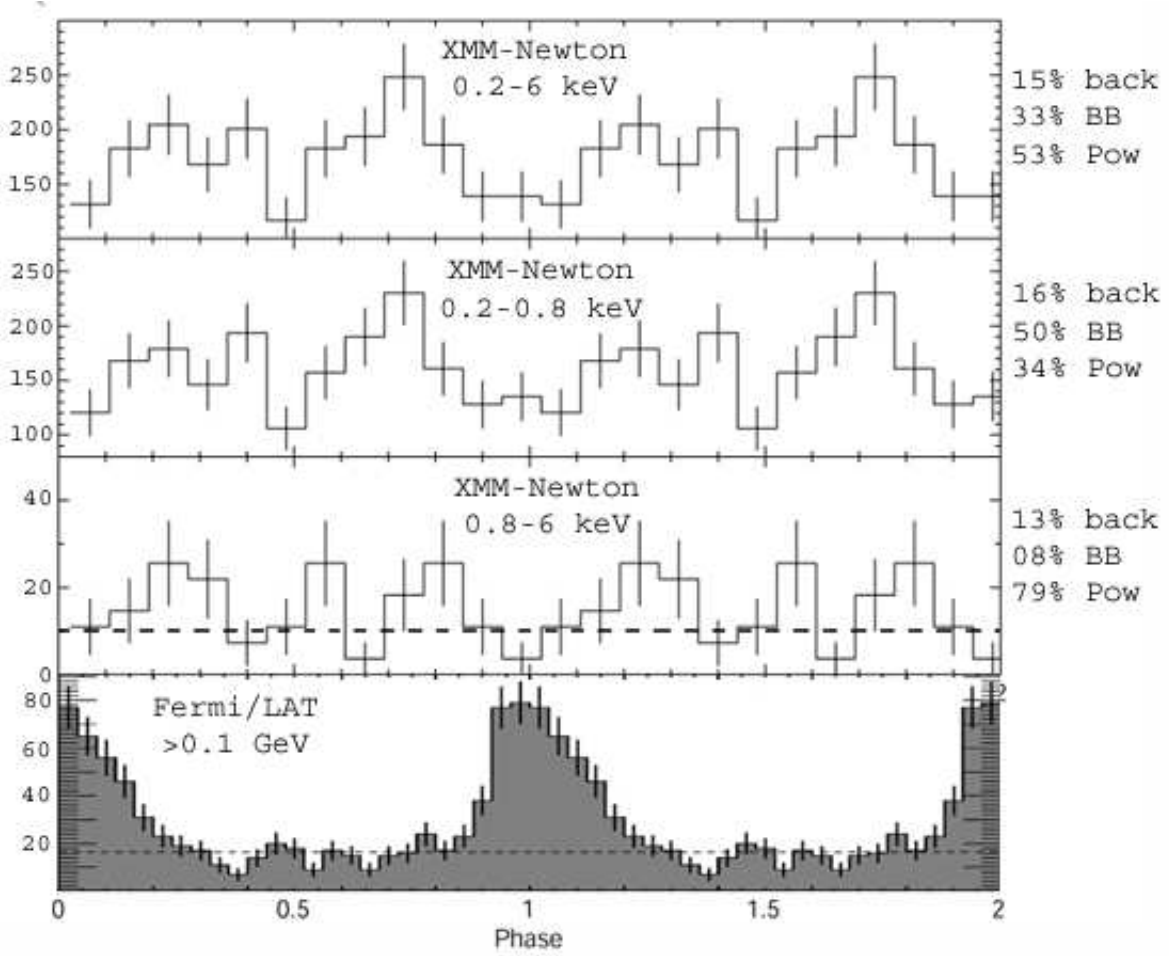


Fig. 3.— EPIC/PN folded light curves in different energy ranges using photons within a 18" radius of the *Chandra* position. X-ray photon phases were computed by folding at the expected period, based on the most recent available LAT ephemeris: the pulsar period at the start of the observation is  $P = 0.44410548661(9)$ s and the  $\dot{P}$  contribution is taken into account. We note that the *XMM-Newton* time slip (discussed in section 3.2) could affect our results. Pattern 0 events have been selected in the 0.2-0.35 keV energy range while Pattern  $\leq 4$  have been used in the 0.35-6 keV range. For each energy band, the relative contributions of all the spectral components are shown. On average the background accounts for  $\sim 15\%$  of the counts. 80% of the 0.8-6 keV counts come from the non-thermal pulsar component while 50% of the 0.2-0.8 keV counts come from the thermal one. The lower panel shows the LAT light curve of the Morla pulsar from Abdo et al. (2010a) to which the *XMM-Newton* light curves have been aligned in phase.

## 4. The Tail

### 4.1. Spatial Analysis

The 2009 *Chandra* observations revealed an extended, bright nebula protruding from the pulsar, extending  $\sim 9'$  in length. Unfortunately, the 2011 *Chandra* observation does not cover the entire nebular emission so it cannot be used. The extended feature can be easily studied in our *XMM-Newton* observation due to its lower particle background and higher spectral resolution, compared to the *Chandra* one. On the other hand, the worse spatial resolution of *XMM-Newton* prevented us from significantly constraining the properties of the nebula near the pulsar. We therefore concentrate on a higher-scale analysis of the extended feature.

First, we produced brightness profiles of the nebula along the pulsar motion (APM) and orthogonal to it (OPM). In order to maximize the statistical significance of each bin, we carefully evaluated the bin size and the width of extraction boxes, choosing a scale of  $90'' \times 50''$  APM and  $450'' \times 12.5''$  OPM (see Figure 4). For each instrument, we excluded the emission region surrounding the pulsar, as well as all the serendipitous sources and CCD gaps, according to our source PSF and calibration studies. Area calculations for each bin take into account the excluded regions. The presence of straylight annuli, PN CCD gaps, and numerous serendipitous sources in the faintest part of the nebula, toward the south-west, forced us to choose ad hoc boxes in that region, in order to exclude all the contaminants.

The brightness profile for both *XMM-Newton* and *Chandra* are shown in figure 5. In order to take into account the different angular resolution of the *XMM-Newton* instruments, the profiles were convolved with a Lorentzian kernel of  $\Gamma = 7.125''$ , corresponding to a full-width half maximum (FWHM) of the distribution of  $6.6''$ , the nominal FWHM of the *XMM-Newton* mirrors. Figure 5 shows the smoothed *Chandra* and *XMM-Newton* brightness



profiles. While minor differences are found in the count rate profiles shown in the figure, taking into account both the different (energy-dependent) effective areas, the flux profiles are compatible. The *XMM-Newton* data show a hint of extended emission, at brightness below the *Chandra* detection limit, near the pulsar itself. Such a difference is possibly due to the higher *XMM-Newton* sensitivity, that highlights the fainter part of the nebula, right behind the pulsar. No variations in the tail profile are detected in the available observations. Along the pulsar motion, the tail emerges from the background within  $50''$  of the pulsar and its flux increases gradually, reaching a flat maximum between  $4'$  and  $7'$ . Its decrease is faster, though the profile is affected by the two serendipitous AGN (see section 2.1) and it fades below the background level at about  $9'$  from Morla. In the direction orthogonal to the main axis (OPM), the tail profile is clearly asymmetric: it shows a fast increase in the northeast direction (rising to the maximum within  $30''$ ), reaches a sharp maximum, in broad agreement with the neutron star proper motion direction, then the decrease is slower, fading at about  $1-1.5'$  in the nearest part of the nebula and  $2'$  in the furthest. Such a behavior recalls the projection of a cone, with the apex corresponding to the pulsar position (or somewhere in the vicinity of the pulsar).

Brightness profiles of the tail in the soft ( $0.3-1.5$  keV) and hard ( $1.5-6$  keV) energy bands show no significant discrepancies, with the possible exception of the region immediately next to the pulsar ( $<50''$ ), where a hint of a softening in the spectrum is seen.

## 4.2. Spectral Analysis

While in the previous *Chandra* observations the spectral analysis of the tail emission was hampered by the low signal-to-noise ratio (S/N) -  $\sim 57\%$  of the total counts coming from the background, - the exceptional sensitivity of *XMM-Newton* allows for a deep study of the nebular emission, with a background contribution of  $\sim 35\%$ .

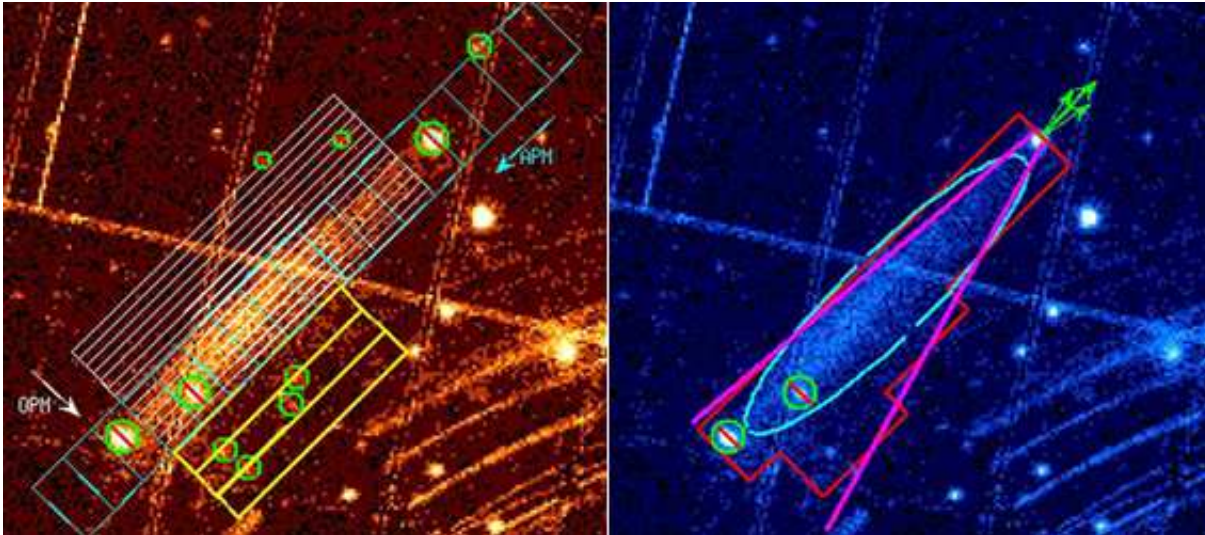


Fig. 4.— 0.3-6 keV exposure-corrected *XMM-Newton* view of the tail, where the PN and two MOS images were added with the `ximage` tool. **Left panel:** The green boxes mark regions used for the brightness profile study along the pulsar proper motion (indicated with an arrow, labeled APM) while white ones mark regions used for the brightness profile study orthogonal to the pulsar proper motion (indicated with an arrow, labeled OPM). Yellow boxes mark the ad-hoc regions used in the region contaminated by straylight annuli. The barred green circles mark regions excluded from the analyses due to the presence of point-like sources. **Right panel:** The red polygon mark the previously defined regions in which the excess due to the presence of the nebula is significant at  $5\sigma$  or more. Following the red polygon, we traced in magenta a plausible shape of the tail while the cyan ellipse is the extraction region used for our spectral analyses on the tail. The long green arrow indicates the direction of the pulsar proper motion, while the two shorter arrows represent the 1 sigma confidence errors on this direction.

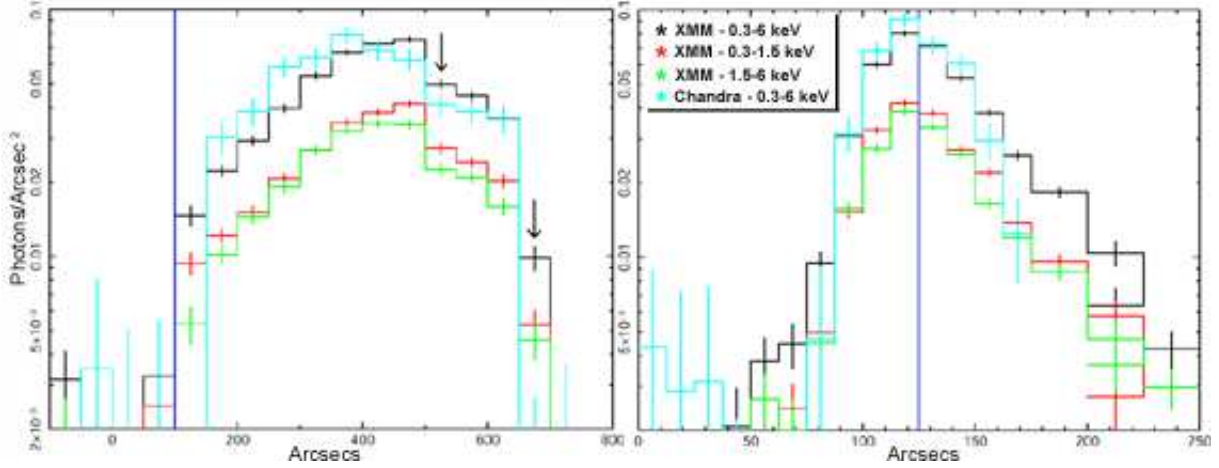


Fig. 5.— Background-subtracted surface brightness profiles of the tail along its main axis (APM, left panel) and orthogonal to it (OPM, right panel). The PN plus MOS profiles in the 0.3-6, 0.3-1.5 and 1.5-6 keV energy ranges are marked, respectively, with black, red, and green. The cyan line shows the smoothed 0.3-6 keV *Chandra* brightness profile. This last has been convolved with a Lorentzian kernel of  $\Gamma = 7.125''$ , corresponding to a Full width at half maximum (FWHM) of the distribution of  $6.6''$ , the nominal FWHM of the *XMM-Newton* mirrors. The integral of the *Chandra* profile has also been normalized to the integral of the 0.3-6 keV *XMM-Newton* one in order to show any possible discrepancy. The blue vertical lines mark the position of the pulsar. Sources 4 and 5, indicated with an arrow, have been removed, possibly enhancing the decrease in brightness. The flat maximum along the main axis is clearly visible between  $\sim 250''$  and  $500''$  as well as the asymmetrical shape of the tail in the direction orthogonal to it. The profiles in the soft and hard X-ray bands are almost the same, with a possible exception right behind the pulsar, where the soft band dominates.

In order to maximize the S/N, we extracted the total spectrum from the brightest part of the nebula, an elliptical region centered at R.A., Dec. (J2000) 03:58:06.59, +32:02:05.42, a semi-major axis of 4' and a semi-minor axis of 50". We excluded from the analysis region a circle with 20" radius around source 5 and the gaps in the CCDs. We extracted the background from source-free circular regions uncontaminated by the extended emission and located on the same CCD as the tail. We generated the response and effective area files using the SAS tools `rmfgen` and `arfgen`. *Chandra* data were treated in the same way as in De Luca et al. (2011) and the resulting spectrum was fitted together with the *XMM-Newton* ones. The spectrum of the nebula is well described ( $\chi^2_\nu = 1.06$ , 162 dof) by a non-thermal emission model (powerlaw with a photon index  $\Gamma = 2.07 \pm 0.08$ ), absorbed by a column  $N_H = (2.61 \pm 0.23) \times 10^{21} \text{ cm}^{-2}$ . Figure 6 shows confidence contours for  $N_H$  and  $\Gamma$  for the diffuse feature and for the pulsar. The value of  $N_H$  obtained for the tail seems to be in conflict (at the  $\sim 3\sigma$  level) with both the one obtained for the pulsar, as well as with the Galactic value, obtained by fitting the spectra of the serendipitous AGNs in the field (see section 2.1). Such a discrepancy between the values of  $N_H$  led us to consider alternative models. The spectrum of the tail is well described ( $\chi^2_\nu = 1.06$ , 162 dof) by a thermal bremsstrahlung model with a temperature  $kT = 3.75^{+0.48}_{-0.40}$  keV, absorbed by the more realistic column  $N_H = (1.72 \pm 0.16) \times 10^{21} \text{ cm}^{-2}$ . Other similar thermal models such as `mekal` (hot diffuse gas Mewe et al. (1985)), `nei` (collisional plasma, non-equilibrium, constant temperature Borkowski et al. (2001)), and `pshock` (plane-parallel shocked plasma, constant temperature Borkowski et al. (2001)) with redshift 0 fit equally well the spectrum of the tail and require a very low metal abundance. Table 2 reports the results of the fit for all the models.

In order to study the spatial-spectral variability of the nebula, we divided the elliptical extraction region using the two axes, then we fitted both the absorbed powerlaw and bremsstrahlung models (see Table 2) for each semi-elliptical region. In this way we obtained

spectra from the semi-elliptical regions nearest to and furthest from the pulsar, and those at the south-west and north-east. No significant ( $3\sigma$ ) variation was detected down to  $\sim 0.2$  in  $\Gamma$  or  $\sim 1$  keV in kT.

## 5. Discussion

### 5.1. The Pulsar

The X-ray spectrum of the Morla pulsar is a combination of thermal radiation from hot spot(s) superimposed on a non-thermal power-law component. A straight estimate of the NS polar cap size, based on a simple centered dipole magnetic field geometry (see e.g. De Luca et al. (2005)) and a standard NS radius of 10 km, predicts in this case a polar cap radius of about 85 m. The observed emitting radius is about 450 m, significantly smaller than the entire surface of any reasonable NS but definitely bigger than the expected polar cap. This is true both using the blackbody model and the NS atmosphere model, although the latter yields a larger emitting area and a lower temperature. Such a large size of the spots has also been found in other well-known pulsars, like PSR B0656+14 and PSR B1055-52 (De Luca et al. 2005), and it is still poorly understood. The luminosity associated with the Morla polar cap is  $1.1 \times 10^{30}$  erg s $^{-1}$ , a factor of a few lower than the luminosity expected from polar caps heated by  $e^{+/-}$  currents. However, it is consistent with the expectations from polar cap heating due to the bombardment by particles created only by inverse Compton scattered photons (Harding & Muslimov 2001, 2002). PSR J0357+3205 is close to the death line for production of  $e^{+/-}$  pairs by curvature radiation photons and this could explain the reduced polar cap heating.

While the majority of X-ray emitting isolated neutron stars (e.g. Kaspi et al. (2006)), exhibit thermal emission coming from the whole NS surface, no such a component is required to fit the *XMM-Newton* spectrum. Using the blackbody model, for a NS radius

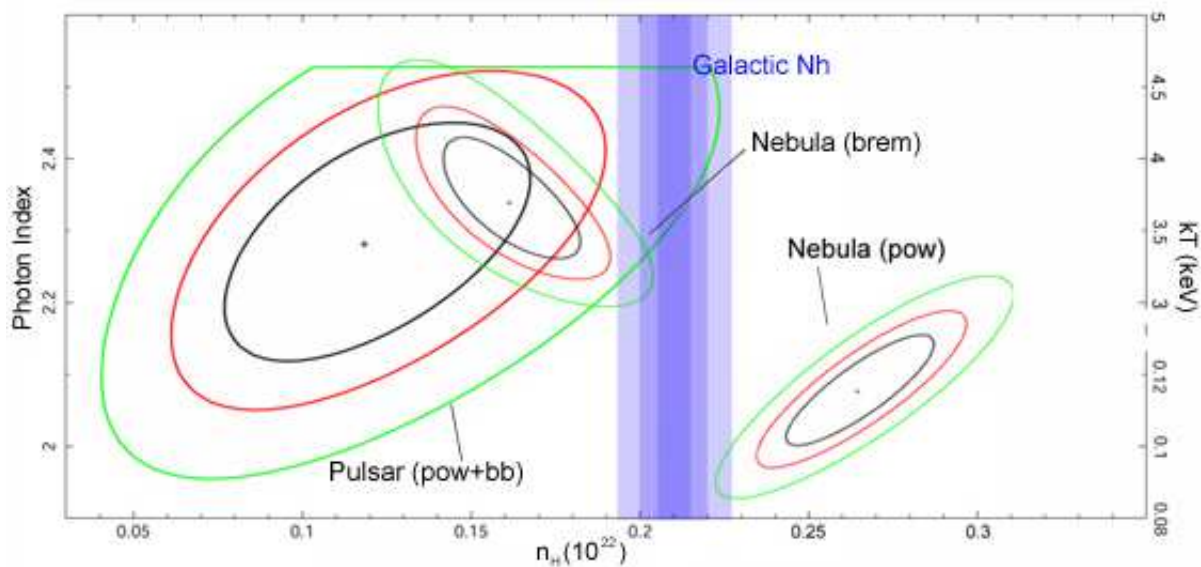


Fig. 6.— Confidence contours from spectroscopy on the pulsar and the tail. Black, red, and green lines respectively show the error ellipses at 68%, 90% and 99% confidence levels for the absorbing column and the photon index. The Galactic  $N_H$  from the study of serendipitous sources (see section 2.1) is also shown with errors at 1, 2, and 3  $\sigma$  indicated by different shades of blue. It is apparent that the Galactic value of  $N_H$  and the value obtained by fitting the powerlaw spectrum on the tail are only marginally compatible.

Table 2: Parameters of different X-ray spectral models of the tail

Model	$\chi^2_\nu$	$N_H$	$\Gamma$	kT	Abund <sup>a</sup>	Flux <sup>b</sup>
		$10^{21} \text{ cm}^{-2}$		keV		$10^{-13} \text{ erg cm}^{-2} \text{ s}^{-1}$
tot-pow	1.06	$2.61 \pm 0.23$	$2.07 \pm 0.08$	-	-	$6.65 \pm 0.40$
tot-brem	1.06	$1.72 \pm 0.16$	-	$3.75^{+0.48}_{-0.40}$	-	$4.95 \pm 0.30$
tot-mek	1.13	$1.73 \pm 0.16$	-	$3.76^{+0.49}_{-0.38}$	<0.099	$4.57 \pm 0.28$
near-brem	1.15	$1.76 \pm 0.14$	-	$4.72^{+0.89}_{-0.69}$	-	$2.23^{+0.20}_{-0.34}$
far-brem			-	$3.39^{+0.38}_{-0.33}$	-	$2.05 \pm 0.16$
sw-brem	1.33	$1.72 \pm 0.14$	-	$4.01^{+0.64}_{-0.52}$	-	$1.83 \pm 0.16$
ne-brem			-	$4.23^{+0.55}_{-0.46}$	-	$2.48 \pm 0.18$

<sup>a</sup>Metal abundances (He fixed at cosmic). The elements included are C, N, O, Ne, Mg, Si, S, Ar, Ca, Fe, Ni, see Anders & Grevesse (1989)

<sup>b</sup>Unabsorbed 0.3-10 keV flux.

Note. — Here we report the best fits of models that can describe the nebular emission. The elliptical extraction region was chosen after an accurate study based on the signal-to-noise ratio. We used an absorbed powerlaw, bremsstrahlung and `mekal`, respectively. Thermal models obtain similar temperatures, absorption columns and abundances. The last four spectra describe the emission from the nearest and the furthest semi-elliptical nebular regions from the pulsar, the south-west and north-east ones, respectively, using a bremsstrahlung model to fit data. To describe the total tail emission, we simultaneously fitted the *XMM-Newton* spectra and the *Chandra* ones. For the different parts of the tail we used only *XMM-Newton* spectra (due to the different PSFs of the two telescopes) and we simultaneously fitted the furthest with the nearest nebular spectra and the south-east with the north-west ones, chaining only the  $N_H$  values. All the errors are at a 90% confidence level.

of 10 km and a distance of 500 pc, the  $3\sigma$  upper limit on the temperature is  $4.4 \times 10^5$  K. This constraint makes Morla the coldest NS in its age range, slightly cooler than the coeval radio-quiet pulsar RX J1856-3754 (e.g. Sartore et al. (2012)). Such a difference can be attributed to different magnetic fields, and thus different magneto-thermal evolution (e.g. Pons et al. (2009)). The non-thermal X-ray luminosity of Morla is in broad agreement with the relation between the X-ray luminosity of rotation-powered pulsars and their spin-down luminosity (Possenti et al. 2002; Kargaltsev et al. 2008; Marelli et al. 2011; Marelli 2012).

## 5.2. The Tail

The morphology of the tail, its spatial extension -  $\sim 1.3$  pc at 500 pc assuming no inclination with respect to the plane of the sky (*i*), - and the lack of any other related Galactic source led De Luca et al. 2011 to associate unambiguously the nebular emission with the pulsar. Elongated X-ray tails coupled with pulsars are quite common (e.g. Kargaltsev & Pavlov (2008a)) and are usually interpreted within the framework of bow-shock, ram-pressure-dominated pulsar wind nebulae (e.g. Gaensler & Slane (2006)). When a pulsar moves supersonically, the shocked pulsar wind is expected to flow in a region downstream of the termination shock (the cavity in the interstellar medium created by the moving Neutron Star and its wind), confined by ram pressure. X-rays are produced by synchrotron emission from the wind particles accelerated at the termination shock, which is typically seen (if it can be resolved) as the brightest part of the extended structure (see, e.g., Kargaltsev & Pavlov (2008b)), according to the expectations from magnetohydrodynamic simulations (Bucciantini 2002; Van der Swaluw 2003; Bucciantini et al. 2005). De Luca et al. (in preparation) have detected and measured a very large proper motion for the pulsar:  $165 \pm 30$  mas yr<sup>-1</sup> -  $390$  km s<sup>-1</sup> across the plane



of the sky, at 500 pc - in the direction opposite to the tail, thus compatible with such a scenario.

The tail shows no other similarities with other, synchrotron-emitting nebulae (for a complete discussion about Morla’s synchrotron-emitting model see De Luca et al. (2011)). The first problem arises from energetic requirements for the emitting particles. According to Goldreich & Julian (1969), the maximum potential drop between the pole and the light cylinder (in an aligned pulsar) is  $\Delta\Phi = (3 \dot{E}_{rot}/2c)^{1/2}$ . In the Morla case, the electrons are accelerated up to a maximum Lorentz factor  $\gamma_{max} \sim 10^8$ , which can be considered as an upper limit for the electrons injected in the pulsar wind nebula. The low  $\dot{E}_{rot}$  of Morla requires an ambient magnetic field as high as  $\sim 50 \mu\text{G}$  - while the mean Galactic value is  $\sim 1 \mu\text{G}$  (Jansson & Farrar (2012) and references therein). However, one must also take into account the magnetic field carried by the particles themselves. An independent estimate of the magnetic field in the tail can be obtained from the measured synchrotron surface brightness (Pavlov et al. 2003). Taking into account the uncertainty on the parameters we can conclude that a reasonable value of the magnetic field in the tail is in the range  $20 - 100 \mu\text{G}$ , consistent with the value of  $\sim 50 \mu\text{G}$  obtained before.

The second problem is the lack of diffuse emission surrounding the pulsar, where the emission from the wind termination shock should be brightest, as observed in all the other known cases (e.g. Gaensler et al. (2004); McGowan et al. (2006); Kargaltsev et al. (2008)). Such a shock could be unresolved by *Chandra* only in the case of an extremely large ambient density (several hundred atoms per  $\text{cm}^3$ ) and/or a pulsar speed higher than some thousands  $\text{km s}^{-1}$ . Taking into account the measure of the proper motion, the distance of the pulsar should be larger than 1.3 kpc or the inclination of the motion should be higher than  $70^\circ$ . Such conditions imply a tail at least 3.5 pc long, so that it becomes even more difficult to account for the energy of the particles. This picture implies also that

a significant fraction of the point-like flux comes from a non-thermal termination shock, reducing dramatically the power-law component of the pulsar. While it is acceptable for the non-thermal component of the pulsar to be a factor of some smaller than the value we obtained (Marelli et al. 2011; Marelli 2012), the lack of nebular emission around the pulsar, where the synchrotron emission should be stronger, remains unexplained.

The brightness profile along the main axis of the tail is consistent with no emission within 30-50'' of the pulsar, then it slowly increases to reach a broad peak at  $\sim 4'$ . This behavior is remarkably different from that observed in all the known synchrotron nebulae that show peaks close to the position of their parent pulsar (e.g. Kargaltsev et al. (2008)), where the acceleration of the wind particles is the most important. It is very hard to explain in this scenario why the emission peaks at  $\sim 1$  pc from the pulsar.

The asymmetric brightness profile of the tail in the direction perpendicular to its main axis is characterized by a sharp northeastern edge and a slow decay toward the south-west direction. The synchrotron emission from the nebula is only marginally dependent on the ISM density, so that ad-hoc and large variations in the ISM are demanded, in order to explain this strange profile. Even if possible, such a case is hardly believable.

Furthermore, the inferred synchrotron cooling time implies a significant spatial-spectral evolution with respect to the distance from the pulsar, as observed in all synchrotron nebulae (Kargaltsev et al. 2008). Thanks to the unique throughput of *XMM-Newton*, we could perform a deep spatial-spectral study of the tail, analyzing separately the furthest and the nearest parts of the nebula. No significant differences in the spectral index are detected (see section 4.2). The lack of variation cannot be easily explained in terms of a synchrotron nebula. The lack of such a softening would require some particle re-acceleration mechanism within the tail itself.

The excellent throughput of the *XMM-Newton* instruments has revealed another problem of the synchrotron nebula scenario, connected to the value of the column density ( $N_H$ )

obtained by fitting the non-thermal model of the nebula. While it is marginally compatible with the value obtained for the pulsar, the inferred  $N_H$  appears to be larger than the Galactic one in that direction, measured by fitting serendipitous AGNs in the field (see Figure 6).

As reported in section 4.2, a thermal bremsstrahlung model fits equally well the spectrum of the tail and produces an estimate of  $N_H$  in agreement with that of the pulsar and the Galactic one. In the bremsstrahlung scenario, the tail emission arises from the shocked ISM material heated up to X-ray temperatures. Under the assumption of a strong shock-wave and from the junction conditions at the shock front, we can estimate the speed of the pulsar directly from the temperature of the shocked ISM material at the head of the bow shock:  $v_{psr} = \sqrt{16kT/(3\mu m_p)}$ , where  $\mu$  is the molecular weight of the ISM gas and we assumed an adiabatic index  $\gamma_{ad} = 5/3$ . The temperature obtained by fitting the tail spectrum with a thermal bremsstrahlung model,  $kT \approx 3.75$  keV, implies a pulsar speed  $v_{psr} \simeq 1376\mu^{-1/2}$  km s<sup>-1</sup>. From the values of the abundances resulting from the spectral fit, we can assume that  $\mu \simeq 0.54$ , so the speed of the pulsar is about 1900 km s<sup>-1</sup>, which would make it the largest ever observed in a pulsar. If we combine this result with the pulsar proper motion we can estimate the inclination angle  $i$  of the pulsar motion (and thus of its tail),  $i \approx \text{acos}(0.2 \times d_{500})$ . Moreover, through the value of the photon flux measured using a thermal bremsstrahlung model, it is possible to estimate the number density of the shocked ISM gas as  $n \simeq 0.86d_{500}^{-1/2}$  atoms cm<sup>-3</sup>.

Thermal bremsstrahlung emission acts as a cooling mechanism. The time scale for cooling can be estimated as  $t_{cool} \simeq (E_{thermal}/J)$ , where  $E_{thermal} \simeq nkT$  is the thermal energy per unit volume and  $J$  is the volume emissivity. This approximation gives  $t_{cool} \simeq 6 \times 10^3 T^{1/2} (n\bar{g}_B)^{-1}$  yr, where  $\bar{g}_B$  is the frequency-averaged Gaunt factor that typically ranges between 1.1 and 1.5, depending on the plasma temperature (Padmanabhan

2000). From our estimates of the temperature and number density of the shocked ISM gas we expect  $t_{cool} \simeq 10^7$  yr. Considering a pulsar proper motion of  $165 \pm 30$  mas yr $^{-1}$  and an extension of the nebula of about 9', then the age of the tail ( $\sim 3300$  yr) is much lower than its cooling time. This result can explain why we have not measured a significant evolution of the temperature of the tail as a function of the distance from the pulsar. On the other hand, the shorter than expected length of the tail can be explained assuming an ad-hoc decrease of a  $\sim 3$  factor in the number density  $n$  beyond the end of the tail - the volume emissivity of the thermal bremsstrahlung emission is  $J \propto n^2 T^{1/2}$ . Such a strong dependence on the ISM density can explain the asymmetrical shape of the nebula in the direction orthogonal to its main axis: this could be a consequence of an inhomogeneity of the number density in the nebula, quite typical in the ISM.

From the conservation of mass, energy, and momentum on the two sides of the shock front and from the values measured in the tail (e.g. the pre-shock temperature  $T_0$  and number density  $n_0$ ), we can calculate the same physical quantities outside the nebula:

$$\frac{n}{n_0} = \frac{(\gamma + 1)M^2}{(\gamma + 1) + (\gamma - 1)(M^2 - 1)} \quad (1)$$

$$\frac{T}{T_0} = \frac{[(\gamma + 1) + 2\gamma(M^2 - 1)][(\gamma + 1) + (\gamma - 1)(M^2 - 1)]}{(\gamma + 1)^2 M^2} \quad (2)$$

where  $M = 1/\sin(\alpha)$  is the Mach number and depends on the cone angle of the tail ( $\alpha$ ) and an adiabatic index  $\gamma_{ad} = 5/3$  is assumed for the ISM gas. In the strong shock-wave limit ( $M \gg 1$ )  $n_0 = n/4 \simeq 0.22 d_{500}^{-1/2}$  atoms cm $^{-3}$  while  $T_0$  depends on the Mach number and thus on the inclination angle  $i$ . From the geometry of the cone angle of the nebula, a plausible value of  $T_0$  is in the range of  $10^5$ - $10^6$  K, for  $i \gtrsim 60^\circ$ . The pre-shock temperature is consistent with that of the hot phase of the ISM, which fills a large fraction of the Galaxy (e.g. Bland-Hawthorn & Reynolds (2000)). Such a scenario is also in full agreement with the requirement of a full ionized ISM by De Luca et al. (in preparation). We note that the density required by our model is slightly higher than expected for the hot ISM: this

may result from the concerted action of massive stellar winds and supernova explosions. Yao & Wang (2005) report the presence of dense ( $10^{-3}$ - $1$  atoms  $\text{cm}^{-3}$ ), hot ( $\sim 10^6$  K) envelopes of gas in our Galaxy. On the other hand, thermal models such as `mekal`, `nei`, and `pshock` point to a very low metallicity of the ISM around the pulsar, making more difficult to explain this dense envelope as the result of a supernova explosion or stellar winds. Future multi-wavelength observations of the field and more detailed Galactic gas models could better constrain and explain the ISM composition around Morla.

A shock-wave scenario can easily explain the lack of diffuse emission surrounding the pulsar. Most of the energy in the pre-shock flow is carried by the ions - the kinetic energy in the streaming of the electrons is less than 1/2000 of the total - but the electrons are generally responsible for the cooling of the plasma: this means that the electron temperature ( $T_e$ ) is responsible for the dynamics of the shock and its emitted spectrum. The electrons must be heated by the ions before the emission becomes detectable and this process takes some time. Coulomb heating of the electrons behind the shock proceeds at a rate

$$\frac{dT_e}{dt} = \frac{T_i - T_e}{t_{eq}} \quad (3)$$

where  $T_i$  is the ion temperature and  $t_{eq} = 7.7(T_e^{3/2}/n)$  s  $\sim 70$  kyr is the equipartition time for a fully ionized plasma with a Coulomb logarithm of 30 (where  $T_e$  is in units of K and  $n$  in  $\text{cm}^{-3}$ ). If all the post-shock energy is in the ions ( $T_e \ll T_i$ ), then the increase in  $T_e$  due to collisional heating follows:  $T_e(coll) = 1.7 \times 10^7 (n_0 t_3 v_{psr8}^2)^{2/5}$  K, where  $t_3$  is the age of the tail in units of  $10^3$  yr,  $n_0$  is the pre-shock number density and  $v_{psr8}$  is the pulsar speed in units of  $10^8$  cm  $\text{s}^{-1}$ . Thus  $T_e(coll) \lesssim 6.6 \times 10^7 d_{500}^{-1/5}$  K, not significantly different from the value observed in the tail. Moreover,  $T_e(coll) \lesssim 5.5 \times 10^6$  K within  $\sim 30''$  of the pulsar (corresponding to  $\sim 200$ - $300$  years, from the measure of the proper motion). This fully explains the lack of diffuse emission surrounding the pulsar.

So far, no evidence of other pulsars characterized by a thermal bremsstrahlung emitting

tail has been reported. This could be explained by the peculiar conditions it requires, e.g. very fast pulsars and an hot and dense ISM. With its estimated velocity of  $1900 \text{ km s}^{-1}$ , J0357+3205 is the fastest moving pulsar known. Among all the pulsars listed in the ATNF Pulsar Catalogue (Manchester et al. 2005), only 2 have a very high velocity ( $\gtrsim 700 \text{ km/s}$ ), reliably measured through an estimate of the distance obtained by other methods than the dispersion measure. PSR B2224+65, powering the Guitar Nebula (Cordes et al. 1993) and showing an X-ray tail similar to Morla (Hui & Becker 2007), has a speed of at least  $865 \text{ km s}^{-1}$  (Manchester et al. 2005). J0821-4300, the central compact object in the Puppis A supernova remnant has a speed possibly higher than  $1000 \text{ km s}^{-1}$  (Hui & Becker 2006; Winkler & Petre 2007; Becker et al. 2012). The spin-down power of PSR B2224+65 is similar to that of Morla ( $\dot{E}_{rot}=5.9 \times 10^{33} \text{ erg s}^{-1}$  and  $1.2 \times 10^{33} \text{ erg s}^{-1}$ ), but the tails are different. While both tails have a similar brightness profile and show no spectral variations, the tail of PSR B2224+65 is misaligned ( $118^\circ$ ) with respect to the proper motion of the pulsar. Alternative explanations have been proposed: according to Bandiera (2008) the feature could be produced by highly energetic particles which escaped the pulsar wind termination shock and are confined by an interstellar magnetic field. This scenario accounts for a faint counter-feature, detected on the opposite side of the pulsar with respect to the tail, but does not explain the absence of spectral variations along the tail (Johnson & Wang 2010). Another possible scenario is that the observed emission comes from a ballistic jet, similar to those of AGNs (Johnson & Wang 2010), but also this picture has some problems. The key to understand why these two pulsars do not emit through thermal bremsstrahlung lies in the ISM characteristics. This emission is detectable in X-rays only if both the ISM density and temperature are high enough ( $\sim 0.2 \text{ atoms cm}^{-3}$  and  $\sim 10^5\text{-}10^6 \text{ K}$ ). It is hardly believable that the ISM around a CCO like J0821-4300, lying inside its supernova remnant, could be denser than  $\sim 10^{-3} \text{ atoms cm}^{-3}$ : this can explain the lack of a bremsstrahlung tail. In the case of PSR B2224+3205, the ISM density, estimated from the  $\text{H}\alpha$  bow-shock

emission to be  $< 1 \text{ cm}^{-3}$  (Chatterjee & Cordes 2002), is lower than the ISM density predicted around Morla. No constraints on the ISM temperature around PSR B2224+3205 appear in the literature: it is not excluded that a low temperature of the ISM may contribute to the lack of a bremsstrahlung tail.

Recently, Tomsick et al. (2012) studied the case of the X-ray source IGR J11014-6103, suggesting an association with the supernova remnant MSH 11-61A (Kesteven 1968), thus inferring a velocity of  $2400\text{-}2900 \text{ km s}^{-1}$ . IGR J11014-6103 shows a complex morphology, consisting of a point source, an elongated tail  $\sim 50''$  long, aligned to the direction of the proper motion, and a feature of  $\sim 4'$ , nearly perpendicular to the proper motion. Spectral and spatial analyses suggest that IGR J11014-6103 could be a pulsar, therefore providing a natural explanation for the co-aligned feature as a bow-shock ram-pressure-confined pulsar wind nebula. Moreover, the feature resembles the tail of Morla: its luminosity peaks far from the pulsar and only a few photons are detected near the pulsar. The low statistics prevent us from studying further the similarities between the two tails. However, if the association with MSH 11-61A is confirmed, its distance would be 10 kpc, implying a tail of  $\sim 2 \text{ pc}$ , comparable to that of Morla.

### 5.3. The Distance and inclination

Our deep *XMM-Newton* observation of the field of J0357+3205 allowed us to better constrain the distance of the pulsar using the interstellar absorption value. The Galactic absorption column in the direction of the pulsar, predicted by Dickey & Lockman (1990) at  $\sim 500 \text{ pc}$  based on the HI distribution, is fully compatible with our best fit value for the pulsar and the tail, pointing to a lower limit for the pulsar distance of  $\sim 300 \text{ pc}$ . This result is in broad agreement with the value estimated by scaling the  $\gamma$ -ray flux of the pulsar (Saz Parkinson et al. 2010): the method hinges upon the observed correlation between the

intrinsic  $\gamma$ -ray luminosity and spin-down power of the pulsar (Abdo et al. 2010a), assuming a beam correction factor of 1 for the  $\gamma$ -ray emission cone of all the pulsars (Watters et al. 2009). By applying this relation, we have a  $\gamma$ -ray efficiency of 0.33 and a distance of  $\sim 500$  pc. We obtain a new upper limit of  $\sim 900$  pc by requiring the  $\gamma$ -ray efficiency to be less than 1.

Another important piece of information could come from the serendipitous stars we found in the field: their distance estimates from optical analyses could provide lower limits on the distance of the pulsar. Future multi-filter optical observations will provide this limit.

Under the hypothesis of a bremsstrahlung-emitting tail, we infer a pulsar velocity of  $\sim 1900$  km s $^{-1}$ . The estimated value of the pulsar proper motion,  $165 \pm 60$  mas yr $^{-1}$ , allows us to set another upper limit for the pulsar distance, being  $2.4_{-0.6}^{+1.4}$  kpc for a purely transversal motion. However, as reported in section 5.2, a null inclination leads to unrealistic values ( $\sim 10^7$  K) of the ISM temperature, so that an inclination angle larger than  $60^\circ$  is required. This lowers the upper limit to  $1.2_{-0.3}^{+0.7}$  kpc, still less constraining than that obtained by computing the pulsar efficiency.

For a pulsar with a kick velocity of  $\sim 1900$  km s $^{-1}$ , a proper motion of  $165$  mas yr $^{-1}$  and a distance of  $300 \text{ pc} < D < 900 \text{ pc}$ , the inclination of the system with respect to the plane of the sky ranges between  $68^\circ$  and  $83^\circ$ , the density of the ISM between 0.15 and 0.3 atoms cm $^{-3}$ , and its temperature between 1 and  $9 \times 10^5$  K. The length of the tail is  $\sim 6.5$  pc, independently of the distance.

Although the study of the kinematics of the pulsar is beyond the scope of this paper, the small component of the proper motion perpendicular to the Galactic plane points to a birth site outside the Galactic plane, suggesting that its progenitor might have been a runaway star, as already introduced in De Luca et al. (2011).



## 6. Conclusions

We have characterized the properties of the middle-aged  $\gamma$ -ray and X-ray pulsar J0357+3205 (Morla) and its tail. The X-ray spectrum of the pulsar is consistent with a magnetospheric non-thermal component plus thermal emission from hot spots; the lack of any detected thermal component from the whole surface makes Morla the coldest NS in its age range.

Folding the X-ray photons at the expected pulsar period using the LAT ephemeris yields marginal evidence for modulation, with 2 peaks, neither of them aligned with the single gamma-ray peak (see Figure 3).

We confirmed the presence of a diffuse emission  $\sim 9'$  long, the largest tail of X-ray emission associated with any rotation-powered pulsar. Such an extended emission cannot be explained in terms of the usual bow-shock ram-pressure-dominated pulsar wind nebula. In fact, the following problems arise:

- the existence of the tail is problematic for a pulsar with such a low  $\dot{E}$  as Morla;
- no bow shock has been resolved around the pulsar;
- the lack of any nebular emission around the pulsar, where the particle acceleration is maximum, cannot be explained;
- the nebular spectrum lacks any spatial evolution, a necessary signature of the radiative cooling of the electrons accelerated at the wind termination shock;
- the very asymmetric brightness profile in the direction perpendicular to the main axis of the tail requires a large ad-hoc inhomogeneity of the ISM around the pulsar;
- fitting the *XMM-Newton* nebular spectra with a powerlaw, we found the nebular  $N_H$  to be higher than the Galactic value and only marginally in agreement with the  $N_H$  of the pulsar.

We propose a thermal bremsstrahlung model as an alternative explanation of the tail emission. In this scenario, the emission comes from the shocked ISM material heated up to

X-ray temperatures. This model gives full account of the peculiar features of the tail:

- the lack of any detectable spatial evolution in the tail spectrum is due to the long bremsstrahlung cool-down time;
- the peculiar asymmetries of the brightness profile can be interpreted in terms of small changes in the ISM density that strongly affect the bremsstrahlung emissivity;
- most of the energy in the pre-shock flow is carried by the ions, while the electron temperature is responsible for the X-ray emission; the Coulomb heating time of the electrons behind the shock is fully in agreement with the lack of any detected nebular emission near the pulsar;
- the value of  $N_H$  measured in the tail agrees both with the value obtained for the pulsar and the Galactic value.

This scenario allows us to estimate some parameters of the pulsar and of the ISM around it. For a bremsstrahlung-emitting tail we estimate the pulsar distance to be between 300 and 900 pc. A pulsar velocity of  $\sim 1900 \text{ km s}^{-1}$  is required, in agreement with the pulsar proper motion for distances of some hundreds parsecs and a high inclination. The mean density of the ISM is required to be  $\sim 0.2 \text{ atoms cm}^{-3}$  and the temperature of some  $10^5 \text{ K}$ . This type of hot gas usually presents lower densities, but a denser phase (possibly detected by Yao & Wang (2005)) is predicted to be the result of the action of massive stellar winds and supernova explosions. However, the low metallicity we obtained from the spectral fit makes the explanation of this gas envelope more difficult.

A high inclination of the system ( $>70^\circ$ ) is predicted in both models. This value provides further support to the bremsstrahlung model, where the cool-down time demands for a longer tail, and adds to the problems of a synchrotron model.

For all these reasons, we believe Morla’s nebula to be the first example of a new “turtle’s tail” class of thermally-emitting nebulae, ironically associated with fast moving pulsars.

Until now we have no clear evidence of other pulsars characterized by a tail emitting via thermal bremsstrahlung, possibly for the requirements of a very fast pulsar and a hot, dense ISM. Moreover, energetic pulsars can also generate classic synchrotron nebulae, that may outshine a bremsstrahlung component. The recently discovered nebula associated with the source IGR J11014-6103, suspected of being a high-velocity pulsar, resembles the tail of Morla: further studies of this feature could lead to a second example of a turtle’s tail nebula.

This work was supported by the contract Swift ASI-INAF 1-004-11-0. We warmly thank the ApJ referee for the useful comments and suggestions as well as the IASF-INAF staff who constructively participated in the discussion during my “Astrosiesta” presentation.

*Facilities:* CXO (ACIS), XMM (EPIC), Mayall (MOSAIC,FLAMINGOS)

## REFERENCES

- Abdo, A.A. et al. 2009, *Science*, 325, 848
- Abdo, A.A. et al. 2009, *Science*, 325, 840
- Abdo, A.A. et al. 2009, *ApJ*, 700, 597
- Abdo, A.A. et al. 2010, *ApJ*, 187, 460
- Anders, E. & Grevesse, N. 1989, *GeCoA*, 53, 197
- Atwood, W.B. et al. 2009, *ApJ*, 697, 1071
- Bandiera, R. 2008, *A&A*, 490, 3
- Becker et al. 2012, *ApJ*, 755, 141
- Bland-Hawthorn, J. & Reynolds, R. 2000, [arXiv:astro-ph/0006058](https://arxiv.org/abs/astro-ph/0006058)
- Borkowski, K.J. et al. 2001, *ApJ*, 548, 820
- Buccheri, R. et al. 1983, *A&A*, 128, 245
- Bucciantini, N., 2002, *A&A* 387, 1066
- Bucciantini, N., et al., 2005, *A&A* 443, 519
- Chatterjee, S. & Cordes, J.M. 2002, *ApJ*, 575, 407
- Cheng, K.S. et al. 1986, *ApJ*, 300, 500
- Cordes, J.M. et al. 1993, *Nature*, 362, 133
- De Luca, A. & Molendi, S. 2004, *A&A*, 419, 837
- De Luca, A. et al. 2005, *ApJ*, 623, 1051

- De Luca, A. et al. 2011, ApJ, 733, 104
- De Luca, A. et al., submitted to ApJ
- Dickey, J.M. et al. 1990, ARA&A, 28, 215
- Gaensler, B.M., et al., 2004, ApJ 616, 383
- Gaensler, B.M. & Slane, P.O. 2006, ARA&A, 44, 17
- Garmire, G.G. et al. 2003, SPIE 4851, 28
- Goldreich, P. & Julian, W.H., 1969, ApJ 157, 869
- Harding, A.K. & Muslimov, A.G., 2001, ApJ 556, 987
- Harding, A.K. & Muslimov, A.G., 2002, ApJ 568, 862
- Harding, A.K. & Muslimov, A.G., 2004, cosp, 35, 562
- Hui, C. Y., & Becker, W. 2006, A&A, 457, L33
- Hui, C.Y. & Becker, W. 2007, A&A 467, 1209
- Hui, C.Y. et al. 2012, ApJ, 747, 74
- Jacoby, G. H. et al. 1998, Proc. SPIE, 3355, 721
- Jager, O.C. & Djannati-Atai, A. 2008, arXiv:0803.0116
- Jansson, R. & Farrar, G.R., 2012, ApJ, 757, 14
- Johnson, S.P. & Wang, Q.D. 2010, MNRAS, 408, 1216
- Kalberla, P.M. et al. 2005, A&A, 440, 775
- Kargaltsev, O. et al. 2008, ApJ, 684, 542

- Kargaltsev O. & Pavlov, G.G., 2008, in AIP Conf. Proc. 983, 171
- Kargaltsev, O. & Pavlov, G.G., 2008, ApJ 684, 542
- Kaspi, V., et al., 2006, in "Compact Stellar X-ray Sources", eds. Lewin, W. and van der Klis, M., Cambridge University Press, p. 279
- Kesteven, M.J.L. 1968, AuJPh, 21, 369
- Kuster, M. et al. 1999, SPIE, 3765, 673
- La Palombara, N. & Mereghetti, S. 2007, A&A, 474, 137
- The LAT collaboration, in preparation "The Second Fermi LAT catalog of  $\gamma$ -ray pulsars"
- Mainieri, V. et al. 2002, A&A, 393, 425
- Manchester, R.N. et al., 2005, AJ, 129, 1993
- Marelli, M. et al. 2011, ApJ, 733, 82
- Marelli, M. 2012, arXiv:1205.1748
- Martin-Carrillo, A. et al. 2012, arXiv:1204.0978
- McGowan, K.E., et al., 2006, ApJ, 647, 1300
- Mewe, R. et al. 1985, A&AS, 62, 197
- Padmanabhan, T. 2000, Teoretical Astrophysics - vol 1, Cambridge University Press
- Pavlov, G.G. et al., 2003, ApJ, 591, 1157
- Pons, J.A. et al. 2009, A&A, 496, 207
- Possenti, A. et al., 2002, A&A, 387, 993

Read, A.M. 2004, XMM-CCF-REL-167

Sartore, N. et al. 2012, A&A, 541, 66

Saz Parkinson, P.M. et al. 2010, ApJ, 725, 571

Struder, L. et al., 2001, A&A, 365, L18

Tomsick, J.A. et al. 2012, ApJ, 754, 145

Turner, M.J.L. et al. 2001, A&A, 365, L27

Van der Swaluw, E., 2003, A&A 404, 939

Watters, K.P. et al., 2009, ApJ, 695, 1289

Winkler, P. F., & Petre, R. 2007, ApJ, 670, 635

Yao, Y. & Wang, Q.D. 2005, ApJ, 624, 751